*energies*

MDPI

*Article*

# Prussian blue analogues based on 3d-metals as cathode materials for magnesium ion batteries

**Andrey Arbenin[1], Semyon Egorov[1], Igor Prikhodko[1], Anna Fedorova[1], Anastasia Penkova[1] and Artem Selyutin[1]***

[1] Saint Petersburg State University, Universitetsky pr.26, Peterhof, Saint Petersburg, 198504, Russia
* Correspondence: a.selyutin@spbu.ru

**Abstract:** Prussian blue PB-analogues $(K;Mg)_xMy[Fe(CN)_6]$ – MHCF were obtained by the co-precipitation method. Mn (MnHCF), Fe (FeHCF), Co (CoHCF), Ni (NiHCF), Cu (CuHCF), Zn (ZnHCF) were selected from transition metals. The obtained substances were characterized by X-ray powder analysis, scanning electron microscopy, thermogravimetric analysis and elemental analysis. An electrochemical study of the obtained cathode materials relative to a metal anode in an aqueous medium was carried out, and the cycling parameters were determined. The influence of 3d-metals nature on the composition-structure-properties of hexacyanoferrates was demonstrated. MHCF are promising cathode materials for $Mg^{2+}$ intercalation/deintercalation in aqueous electrolytes.

**Keywords:** magnesium ion batteries; intercalation; Prussian blue; cathode materials.

## 1. Introduction

In the 21st century, analogues of Prussian blue with various transition metal atoms have found applications in areas such as hydrogen storage [1, 2], electrochromic materials [3], wastewater treatment [4], photomagnetic materials [5] and biomedicine [6]. These compounds can also act as catalysts for organic synthesis [7, 8] and as precursors for the synthesis of nanoscale oxides [9, 10]. In the last 10 years, the direction of using transition metal ferrocyanides as cathode materials for water batteries has been actively developed [11]. The cubic structure of Prussian Blue analogues, with a rigid framework of transition metal atoms and a network of open channels for diffusion, promotes reversible intercalation/deintercalation of both monovalent [12] and multivalent ions [13]. The low deformation of the crystal lattice during ion exchange ensures high citation. Other advantages of these compounds include high theoretical capacity, low cost, scalability and environmentally friendly synthesis [14]. In addition, by introducing transition metal atoms capable of redox reaction in aqueous solution into the ferrocyanides, it is possible to further increase the battery capacity [15]. Most transition metal ferrocyanides reported in the literature have micron-sized particles, which is not the optimal morphology for ion diffusion [16]. Today, lithium-ion batteries are widely used as energy storage devices. They have high power, sufficient cycling efficiency and stable operation [17]. On the other hand, the use of lithium-ion technologies for large-scale applications is very difficult, mainly due to the low stability of lithium in the atmosphere. In addition, lithium is characterized by high cost, small and uneven distribution of reserves in the Earth's crust [18]. Most of the lithium reserves are located in South America, so the production of lithium-ion batteries in our country depends on imports. Magnesium is more stable in the atmosphere, so magnesium-ion batteries can work on the basis of aqueous electrolytes, which is more environmentally friendly and safer [19]. At the same time, magnesium has similar properties to lithium due to the proximity of the ionic radii. On the other hand, the charge of magnesium is twice as high, which gives its advantage in volume capacity [20]. Despite all these positive characteristics, the development of magnesium-ion technology is

**Citation:** To be added by editorial staff during production.

Academic Editor: Firstname Lastname

Received: date
Revised: date
Accepted: date
Published: date

lagging behind that of lithium. The bivalent nature of magnesium slows down the kinetics of ion diffusion through inorganic cathode materials, resulting in low reversibility and low power. Recent work shows that the low mobility of magnesium ions is due to both strong ionic interactions and redistribution of divalently charged cations in the electrode material [21]. Several strategies have been proposed to overcome this problem:

1. Use compounds with high divalent ion mobility as cathode materials [22, 23];
2. Reducing the diffusion length of magnesium ions by using nanoscale and mesoporous materials [24].

Transition metal ferrocyanides have already been well established as cathode materials for lithium and sodium ion batteries [25, 26]. The number of publications on these systems has not diminished to date. Due to structural features, Prussian blue analogues can intercalate/deintercalate multivalent ions such as $Mg^{2+}$, $Ca^{2+}$, $Sr^{2+}$, $Ba^{2+}$, $Zn^{2+}$, $Al^{3+}$, indicating a sufficiently high mobility of multivalent ions in the electrode material [27]. As the development of technologies based on multivalent ions is a relatively recent direction, there are few articles devoted to this topic. There are only three papers in the literature on the study of the behavior of transition metal ferrocyanides in aqueous solutions of magnesium salts, where the data are rather descriptive [28−30]. Therefore, there is a need for fundamental research on such systems. The popularity of transition metal ferrocyanides as cathode materials for water batteries is due to a number of reasons. Firstly, the properties of the cathode material based on these compounds can be adjusted by changing the composition, morphology and particle size of the substance. Secondly, transition metal ferrocyanides are similar in nature to zeolites and can intercalate alkaline and alkaline earth cations in an aqueous solution without destroying the crystal structure [31]. Thirdly, the synthesis of these compounds is inexpensive and the materials themselves are safe to use and non-toxic [32].

In this paper we present our systematic study of influence various 3d-metals nature on the electrochemical properties of PB-analogues as cathode materials for magnesium ion batteries. They have high ionic conductivity that justifies their voltage limited in aqueous electrolyte.

## 2. Materials and Methods

### *2.1. Synthesis*

All chemicals were grade pure for analysis and used without further purification. The preparation of MHCF (M = Mn, Fe, Co, Ni, Cu, Zn) was done using a solution precipitation method. Typically, 40 mL 20 mM $K_3Fe(CN)_6$ aqueous solution and 40 mL 40 mM $M(NO_3)_2 \cdot 6H_2O$ (M = Cu, Co, Fe, Ni, Mn, Zn) aqueous solution was slowly added to 20 mL deionized water at a rate of 1 ml·min-1 under continuous stirring at 343 K. The resulting solution was kept at room temperature for 18 h. The resulting precipitate was dried in an oven at 333 K for 6 h.

After the precipitate MHCF (M = Mn, Ni, Zn) was filtered, washed many times with deionized water. The precipitate MHCF (M = Fe, Co, Cu) resisted centrifugation at 13000 rpm during 3 min that was necessary to force its precipitation. After the preparation the precipitate was washed with deionized water and centrifuged again. The procedure was repeated 5 times.

### *2.2. Materials' characterization*

The crystalline structure of the sample was characterized by the powder X-ray diffraction method (XRD) on a Bruker D2 Phaser Diffractometer with Cu K$\alpha$ radiation over the 2$\Theta$ range of 5−80°. Theoretical models were constructed to refine the structure of compounds by the Rietveld's method in the program «Topas 4.2». The size and morphological appearance of the powder were observed by the scanning electron microscopy (SEM) on the Hitachi S-3400N in a secondary electron registration mode with an accelerating voltage of 20 kV. Thermal material testing was performed on SETSYS Evolution 16 in the

temperature range from room temperature to 700 K. The chemical composition of the PB-analogues was determined inductively coupled plasma (ICP method) in a solution of nitric acid. The measurements were performed on Shimadzu ICPE-9000. The studies were performed using the equipment and Resource Centers of Science Park Saint Petersburg State University.

### *2.3. Electrochemical measurements*

Electrochemical intercalation and deintercalation of Mg ions were performed by using a three-electrode cell. The working electrodes were fabricated by mixing 80 wt.% MHCF, 7 wt.% polyvinylidene fluoride (Kynar), 13 wt.% graphite and grinding the components together with a mortar and pestle. The powder was mixed with 1-methyl-2-pyrrolidinone (PVDF) to create a slurry that was deposited on to steel or platinum foils. These electrodes were dried under vacuum at 353 K and exhibited a typical mass loading of approximately 8 mg/cm$^2$. AgCl/Ag was used as the reference electrode and the counter electrode was steel or platinum. For the electrolyte, an aqueous solution of 1 M $MgSO_4$ was used. Cyclic voltammetric measurements were carried out at a scanning rate of 1 mV/s. Working range of the potential was from 2.35 to 3.55 V vs. Mg2+/Mg. The electrochemical behavior of MHCF was tested in galvanostatic charge/discharge mode using a potentiostat-galvanostat P-30SM Elins.

## 3. Results and Discussion

### *3.1. X-ray diffraction*

Full profile powder X-ray diffraction analyses of the samples were performed on a Bruker D2 phaser diffractometer (Cu K$\alpha$) with precise identification of cell parameters by the Rietveld method. MHCF were found to have a different crystal structure, although they were obtained under identical synthesis conditions.

The cubic MnHCF, FeHCF, CoHCF, NiHCF, CuHCF have a space group Fm-3m (Figure 1). PB analogues with copper and manganese were well crystallized. The broadening of peaks in the X-ray diffraction of NiHCF, FeHCF and CoHCF may be due to a decrease in particle size or microdeformations of the structure. A small amount of amorphous impurity is present in FeHCF and CoHCF as evidenced by the appearance of a halo at small diffraction angles. The trigonal ZnHCF has a space group of R-3c. The resulting sample is well crystallized and has no crystalline impurities (Table 2, 3). Figure 1 shows the experimental results for a full profile powder X-ray diffraction analysis of the samples.

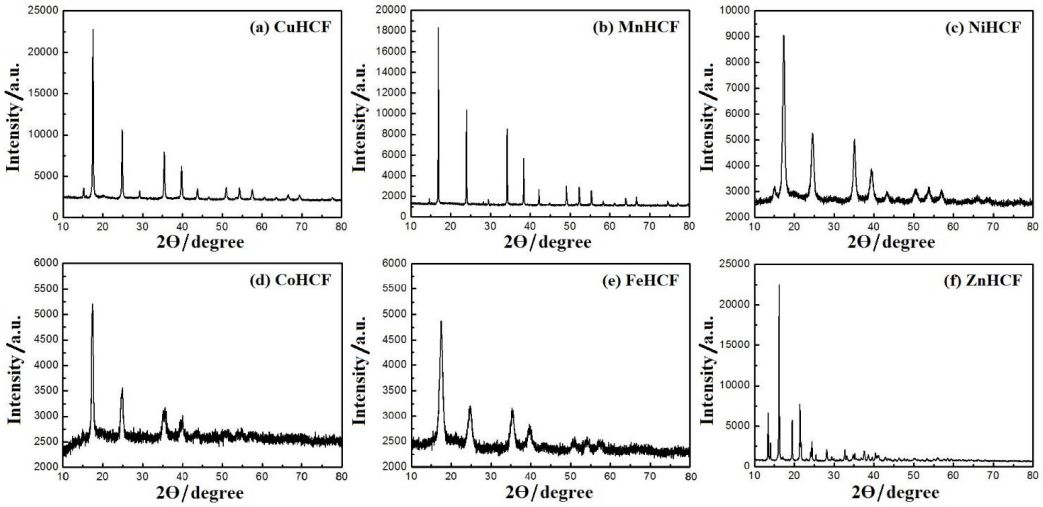


**Figure 1.** X–ray diffraction of PB-analogues: (a) Cu, (b) Mn, (c) Ni, (d) Co, (e) Fe, (f) Zn.

Structural parameters (coordinates and population of atoms, unit cell parameters, texture) were refined by the Rietveld method from the powder X-ray diffraction data (Table 1, Table 2). The structure of $Ni_4[Fe(CN)_6]_{2.67}{\cdot}21H2O$ (№151705 − ICSD) was chosen as a theoretical model for MHCF with a cubic structure. The structure of ZnHCF was refined based on the structure of $Zn_3[Fe(CN)_6]_2$ (157850 − ICSD) with space group R-3c.

**Table 1.** Experimental data of the crystal structure for MHCF.

| | **MnHCF** | **FeHCF** | **CoHCF** | **NiHCF** | **CuHCF** | **ZnHCF** |
|---|---|---|---|---|---|---|
| R-Bragg ($R_B$) | 2.78 | 0.30 | 4.66 | 1.25 | 2.00 | 3.30 |
| Crystal system | Cubic | Cubic | Cubic | Cubic | Cubic | Trigonal |
| Space group | Fm-3m | Fm-3m | Fm-3m | Fm-3m | Fm-3m | R-3c |
| Cell Mass | 1044.5 | 1095.2 | 1213.7 | 1238.9 | 1356.1 | 3720.4 |
| Cell Volume ($Å^3$) | 1156.3 | 1049.6 | 1021.8 | 1067.1 | 1035.2 | 4543.1 |
| Wt% − Rietveld | 100.0 | 100.0 | 100.0 | 100.0 | 100.0 | 100.0 |
| *a* (Å) | 10.492 | 10.106 | 10.097 | 10.219 | 10.107 | 12.648 |
| c (Å) | – | – | – | – | – | 32.647 |

**Table 2.** Refinement parameters of crystalline cell by Rietveld's method. It contains information on atomic parameters, such as coordinates and population. The value of $R_{exp}$-factor indicates the level of agreement between the experimental data and the calculated radiograph.

| **Sample** | **Site** | **Pos.** | ***x*** | ***y*** | ***z*** | **Atom** | **Site population** | **$R_{exp}$** | **$R_B$** |
|---|---|---|---|---|---|---|---|---|---|
| | Mn1 | 4 | 0.5000 | 0.0000 | 0.0000 | $Mn^{2+}$ | 0.852 | | |
| | Fe1 | 4 | 0.0000 | 0.0000 | 0.0000 | $Fe^{3+}$ | 0.666 | | |
| | C1 | 24 | 0.1880 | 0.0000 | 0.0000 | C | 0.666 | | |
| MnHCF | N1 | 24 | 0.2997 | 0.0000 | 0.0000 | N | 0.666 | 3.16 | 2.78 |
| | O1 | 24 | 0.2889 | 0.0000 | 0.0000 | $O^{2-}$ | 0.001 | | |
| | O2 | 32 | 0.1860 | 0.1860 | 0.1860 | $O^{2-}$ | 0.187 | | |
| | O3 | 8 | 0.2500 | 0.2500 | 0.2500 | $O^{2-}$ | 2.574 | | |
| | Fe2 | 4 | 0.5000 | 0.0000 | 0.0000 | $Fe^{2+}$ | 0.808 | | |
| | Fe1 | 4 | 0.0000 | 0.0000 | 0.0000 | $Fe^{3+}$ | 0.666 | | |
| | C1 | 24 | 0.1880 | 0.0000 | 0.0000 | C | 0.666 | | |
| FeHCF | N1 | 24 | 0.2997 | 0.0000 | 0.0000 | N | 0.666 | 1.97 | 0.30 |
| | O1 | 24 | 0.2889 | 0.0000 | 0.0000 | $O^{2-}$ | 0.002 | | |
| | O2 | 32 | 0.1860 | 0.1860 | 0.1860 | $O^{2-}$ | 0.306 | | |
| | O3 | 8 | 0.2500 | 0.2500 | 0.2500 | $O^{2-}$ | 0.452 | | |
| | Co1 | 4 | 0.5000 | 0.0000 | 0.0000 | $Co^{2+}$ | 0.904 | | |
| | Fe1 | 4 | 0.0000 | 0.0000 | 0.0000 | $Fe^{3+}$ | 0.666 | | |
| | C1 | 24 | 0.1880 | 0.0000 | 0.0000 | C | 0.666 | | |
| CoHCF | N1 | 24 | 0.2997 | 0.0000 | 0.0000 | N | 0.666 | 2.47 | 4.66 |
| | O1 | 24 | 0.2889 | 0.0000 | 0.0000 | $O^{2-}$ | 0.002 | | |
| | O2 | 32 | 0.1860 | 0.1860 | 0.1860 | $O^{2-}$ | 0.298 | | |
| | O3 | 8 | 0.2500 | 0.2500 | 0.2500 | $O^{2-}$ | 0.335 | | |

| | | | | | | | | | |
|---|---|---|---|---|---|---|---|---|---|
| NiHCF | Ni1 | 4 | 0.5000 | 0.0000 | 0.0000 | $Ni^{2+}$ | 0.919 | 1.98 | 1.25 |
| | Fe1 | 4 | 0.0000 | 0.0000 | 0.0000 | $Fe^{3+}$ | 0.666 | | |
| | C1 | 24 | 0.1880 | 0.0000 | 0.0000 | C | 0.666 | | |
| | N1 | 24 | 0.2997 | 0.0000 | 0.0000 | N | 0.666 | | |
| | O1 | 24 | 0.2889 | 0.0000 | 0.0000 | $O^{2-}$ | 0.027 | | |
| | O2 | 32 | 0.1860 | 0.1860 | 0.1860 | $O^{2-}$ | 0.328 | | |
| | O3 | 8 | 0.2500 | 0.2500 | 0.2500 | $O^{2-}$ | 0.466 | | |
| CuHCF | Cu1 | 4 | 0.5000 | 0.0000 | 0.0000 | $Cu^{2+}$ | 0.906 | 2.50 | 2.00 |
| | Fe1 | 4 | 0.0000 | 0.0000 | 0.0000 | $Fe^{3+}$ | 0.666 | | |
| | C1 | 24 | 0.1880 | 0.0000 | 0.0000 | C | 0.666 | | |
| | N1 | 24 | 0.2997 | 0.0000 | 0.0000 | N | 0.666 | | |
| | O1 | 24 | 0.2889 | 0.0000 | 0.0000 | $O^{2-}$ | 0.006 | | |
| | O2 | 32 | 0.1860 | 0.1860 | 0.1860 | $O^{2-}$ | 0.158 | | |
| | O3 | 8 | 0.2500 | 0.2500 | 0.2500 | $O^{2-}$ | 0.285 | | |
| ZnHCF | Fe1 | 12 | 0.0000 | 0.0000 | 0.1466 | $Fe^{3+}$ | 1.000 | 3.12 | 3.30 |
| | Zn1 | 18 | 0.2900 | 0.0000 | 0.2500 | $Zn^{2+}$ | 1.000 | | |
| | C1 | 36 | 0.1159 | -0.0150 | 0.1797 | C | 1.000 | | |
| | N1 | 36 | 0.1811 | -0.0230 | 0.2028 | N | 1.000 | | |
| | C2 | 36 | 0.1302 | 0.1161 | 0.1133 | C | 1.000 | | |
| | N2 | 36 | 0.2163 | 0.1906 | 0.0969 | N | 1.000 | | |

The morphology and particle size distribution also depend on the nature of the transition metals. Scanning electron microscopy (SEM) was used to obtain images on the Hitachi S-3400N. The experimental data obtained, shown in Figure 1, are in agreement with the results of X-ray phase analysis.

### *3.2. X-ray diffraction*

SEM images were obtained reflecting the particle morphology for all synthesized compounds, see Figure 2.

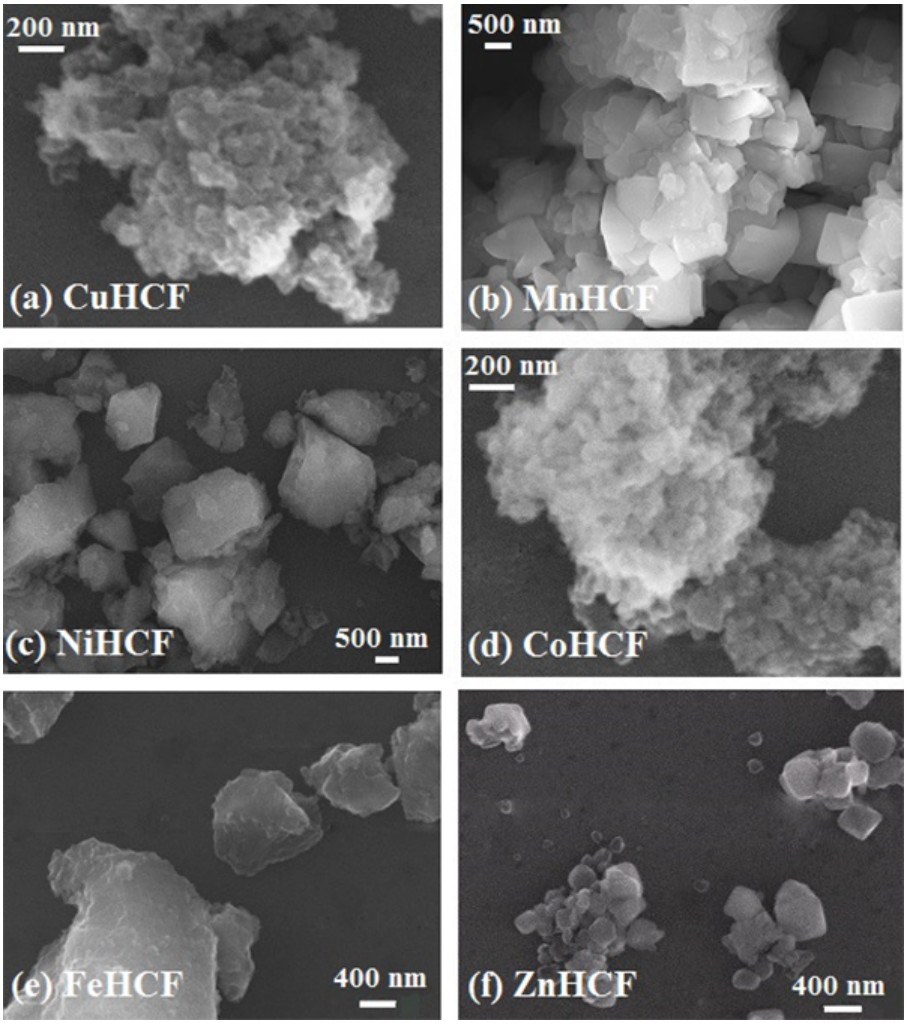


**Figure 2.** SEM images of PB-analogues.

The particle size distribution was constructed from images. A minimum of 30 particles were selected for each compound and the particle size distribution shown in Figure 3 was constructed.

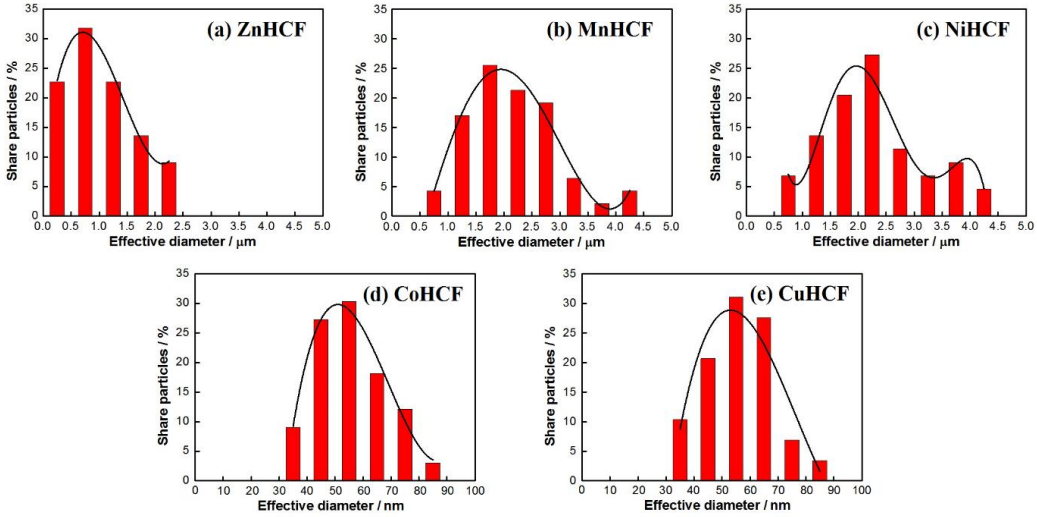


**Figure 3.** Particle size distribution.

### *3.3. Thermal analysis*

Thermal studies of synthesized samples were carried out to determine the number of water molecules in the complexes. According to the literature, in the structure of PB analogues it is possible that water molecules are adsorbed on the surface or intercalated into the lattice cavity, which is confirmed by the TGA-DTG diagram in Figure 4.

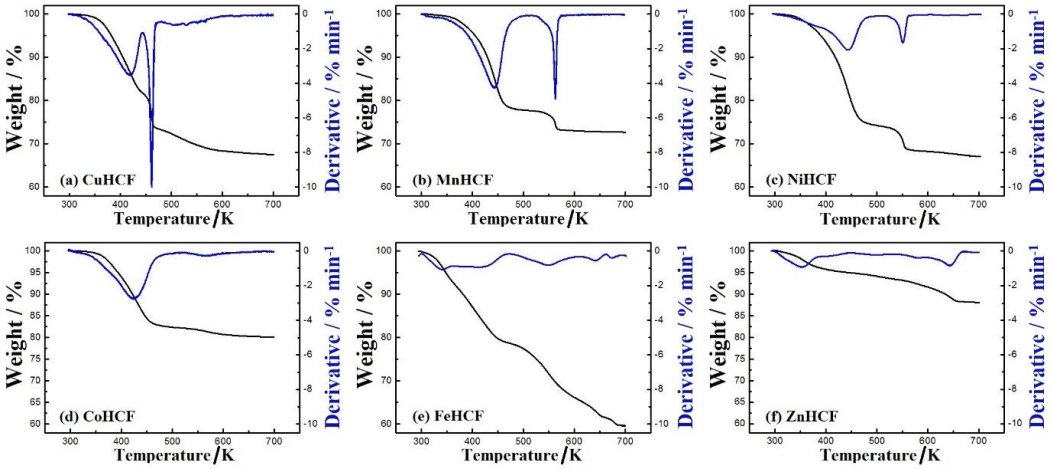


**Figure 4.** TGA results for the PB-analogues with: (a) Cu, (b) Mn, (c) Ni, (d) Co, (e) Fe, (f) Zn. The black color lines show a decrease in the mass of the sample in percentage, the blue color lines depict time derivative.

### *3.4. Chemical analysis*

Elemental analysis was carried out to determine the compound formula using the ICP. Powder samples of the PB analogues were subjected to microwave decomposition in nitric acid to obtain a solution. The mass contents of the metals are given in Table 3.

**Table 3.** Results of the chemical analysis of compounds in mol.%.

| Designation | K | Mn | Fe | Co | Ni | Cu | Zn |
|---|---|---|---|---|---|---|---|
| MnHCF | 5.9 | 54.4 | 39.8 | – | – | – | – |
| FeHCF | – | – | 100 | – | – | – | – |
| CoHCF | – | – | 38.7 | 61.3 | – | – | – |
| NiHCF | 3.2 | – | 38.5 | – | 58.3 | – | – |
| CuHCF | 3.6 | – | 36.7 | – | – | 59.7 | – |
| ZnHCF | – | – | 36.3 | – | – | – | 63.7 |
| MnHCF | 5.9 | 54.4 | 39.8 | – | – | – | – |
| FeHCF | – | – | 100 | – | – | – | – |

**Table 4.** Summary data based on chemical analysis and thermal testing.

| Designation | The formula of compound | K+ vs. $M^{2+}$, mol. % | Amount of zeolitic water |
|---|---|---|---|
| MnHCF-1 | $K_{0.21}Mn_{1.39}Fe(CN)_6 \cdot 4H_2O$ | 15.11±0.30 | 1 |
| FeHCF-1 | $Fe_{1.50}Fe(CN)_6 \cdot 6H_2O$ | – | – |
| CoHCF-1 | $Co_{1.50}Fe(CN)_6 \cdot 3H_2O$ | – | – |

| | | | |
|---|---|---|---|
| NiHCF-1 | $K_{0.12}Ni_{1.44}Fe(CN)_6 \cdot 6H_2O$ | 8.33±0.16 | 2 |
| CuHCF-1 | $K_{0.14}Cu_{1.43}Fe(CN)_6 \cdot 6H_2O$ | 9.79±0.20 | 1 |
| ZnHCF-1 | $Zn_{1.50}Fe(CN)_6$ | – | – |

### *3.5. Electrochemical experiments*

The experimental specific capacity ($Q_{exp}$) was calculated by integrating the cathode branch on a cyclic voltammograms obtained at a scanning speed of 1 mV/ s.

**Table 5.** The results of the electrochemical behavior of the synthesized samples in aqueous solution 1M $MgSO_4$ vs. $Mg^{2+}$/Mg.

| **Element** | **$E_{ox}$ (V)** | **$E_{red}$ (V)** | **$Q_{calc}$ (mAh g$^{-1}$)** | **$Q_{exp}$ (mAh g$^{-1}$)** |
|---|---|---|---|---|
| CuHCF | 3.45 | 2.88<br>2.51 | 64.3 | 21.0 |
| NiHCF | 3.10 | 2.81<br>2.47 | 65.4 | 19.2 |
| MnHCF | 3.15 | 2.84<br>2.67 | 72.7 | 9.8 |
| CoHCF | 3.15 | 2.49 | 75.6 | 6.1 |
| FeHCF | 3.47 | 2.63 | 66.3 | 1.5 |
| ZnHCF | 3.42 | 2.56 | 86.6 | 2.4 |

For example, the image of MnHCF shows sufficiently large crystals of cubic shape with an average size of 2.5 ± 1.7 μm. The combination of small particles into large agglomerates with sizes ranging from 0.5 to 4.5 μm is characteristic of NiHCF. The particle sizes of CoHCF and CuHCF are in the nanometer range. Their average size is between 35 and 85 nm. The geometric parameters of the agglomerates obtained for FeHCF could not be measured. The large particles in the image are probably a cluster of smaller particles (Figure 3).

Due to the size of the zeolitic channels in the cubic crystal lattice of hexacyanoferrates, they can allocate not only alkali and alkaline earth metal cations [30, 33–35], but also water molecules. According to the literature, PB analogues can contain two types of water molecules: adsorbed on the surface and intercalated in zeolitic channels [26]. As the samples dry, the adsorbed water molecules evaporate first and then the number of intercalated molecules begins to decrease. The role of water molecules in the composition of PB analogs is still poorly understood. For example, Yang [36] states that the presence of zeolitic water has no significant effect on the electrochemical properties of cathode materials. However, in a number of other studies, researchers argue that the molecules of zeolitic water improve the diffusion kinetics by shielding the charge of the cations [37–39].

Thermal studies were carried out on SETSYS Evolution 16 in the temperature range from room temperature to 700 K. In accordance with theoretical ideas, the results obtained can be interpreted as follows. The decrease in mass of the sample in the temperature range 413-463 K indicates the evaporation of surface adsorption water (Figure S4). Zeolitic water probably evaporates at higher temperatures from 553 to 585 K, with one mole of zeolitic water per mole of the compound in the hexacyanoferrates MnHCF and CuHCF. The amount of zeolitic water increases to 2 moles in NiHCF. Zeolitic water is absent in FeHCF, CoHCF and ZnHCF samples.

The chemical composition of the synthesized PB analogues was determined by atomic emission spectroscopy with inductively coupled plasma on Shimadzu ICPE-9000

(Tables 4, 5). The presence of $K^+$ in the hexacyanoferrates allows the intercalation of alkali and alkaline earth metal cations into the zeolitic sites. At the same time, water molecules preferentially pass through the compounds in which K+ is absent [27, 40]. In MnHCF, NiHCF and CuHCF, part of the 3d metal cations in the sites of the cubic crystal lattice are replaced by $K^+$. The composition of these compounds is given by the formulae $K_{0.14}Cu_{1.43}Fe(CN)_6 \cdot 6H_2O$, $K_{0.12}Ni_{1.44}Fe(CN)_6 \cdot 6H_2O$ and $K_{0.21}Mn_{1.39}Fe(CN)_6 \cdot 4H_2O$. FeHCF, CoHCF and ZnHCF do not contain $K^+$ in their composition. The molecular formula of these compounds is $Co_{1.50}Fe(CN)_6 \cdot 3H_2O$, $Fe_{1.50}Fe(CN)_6 \cdot 6H_2O$ and $Zn_{1.50}Fe(CN)_6$. The structure of the PB analogues, in which there are no alkali metal cations, becomes defective due to the presence of vacancies at the sites of the cubic crystal lattice.

The electrochemical behavior of cathode materials in an aqueous solution of 1M $MgSO_4$ has been studied using the method of cyclic voltammetry on an Elins P-30SM potentiostat. The reaction that takes place during the intercalation of $Mg^{2+}$ into the zeolitic channels of the cubic crystal lattice can be described as follows,

$$M_3^{2+}[Fe^{3+}(CN)_6]_2 + 2xe^- + xMg^{2+} = Mg_x^{2+}M_3^{2+}[Fe_{(1-x)}^{3+}Fe_x^{2+}(CN)_6]_2$$

In the course of the experiment, it was found that the second maximum in the cathode region is observed on the voltammogram for cathode materials obtained on the basis of MHCF in the presence of $K^+$ (Figure 5(a)). A similar picture is also observed for MnHCF and CuHCF. A maximum reflecting the recovery reaction can be seen on the voltammograms of FeHCF, CoHCF and ZnHCF, as shown in the example of a CoHCF in Figure 5(b).

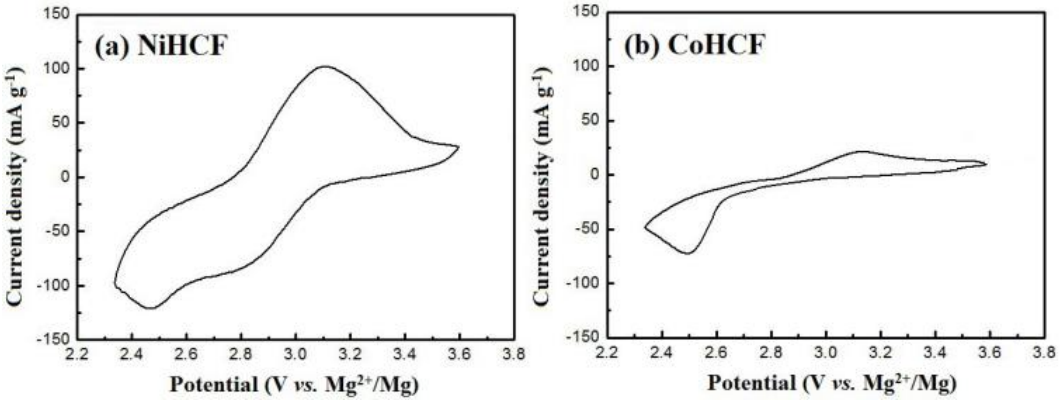


**Figure 5.** Cyclic voltammograms of PB-analogues with (a) nickel and (b) cobalt.

The appearance of a second maximum in the cathode region requires additional study of the mechanism of magnesium intercalation, which is beyond the scope of this study. According to scientists studying the intercalation of multiply charged ions in a cubic crystal lattice, the appearance of an additional wave indicates the process of desorption of an alkali metal cation during the intercalation of highly charged ions [41−44].

The desorption of $K^+$ takes place at a potential of 2.8 V for the example of a NiHCF voltammogram. The results of the electrochemical study for all synthesized MHCF are presented in Table 6, which also includes theoretical and experimental specific capacitance values.

The theoretical specific capacitance ($Q_{calc}$) was calculated on the assumption that 1 electron participates in the reaction, according to the formula $Q_{calc} = (nF)/M$, where n is the number of electrons participating in the electrochemical reaction, F = 96485.3 C/mol is the Faraday constant, M is the molar mass of the compound in g/mol.

The large difference between the theoretical and experimental capacitance indicates that a smaller number of electrons are involved in the intercalation process. The presence of part of the amorphous phase, which does not participate in the electrochemical reaction,

can also reduce the capacitance value. It should be noted that the samples containing potassium ions showed a large capacitance during the experiment.

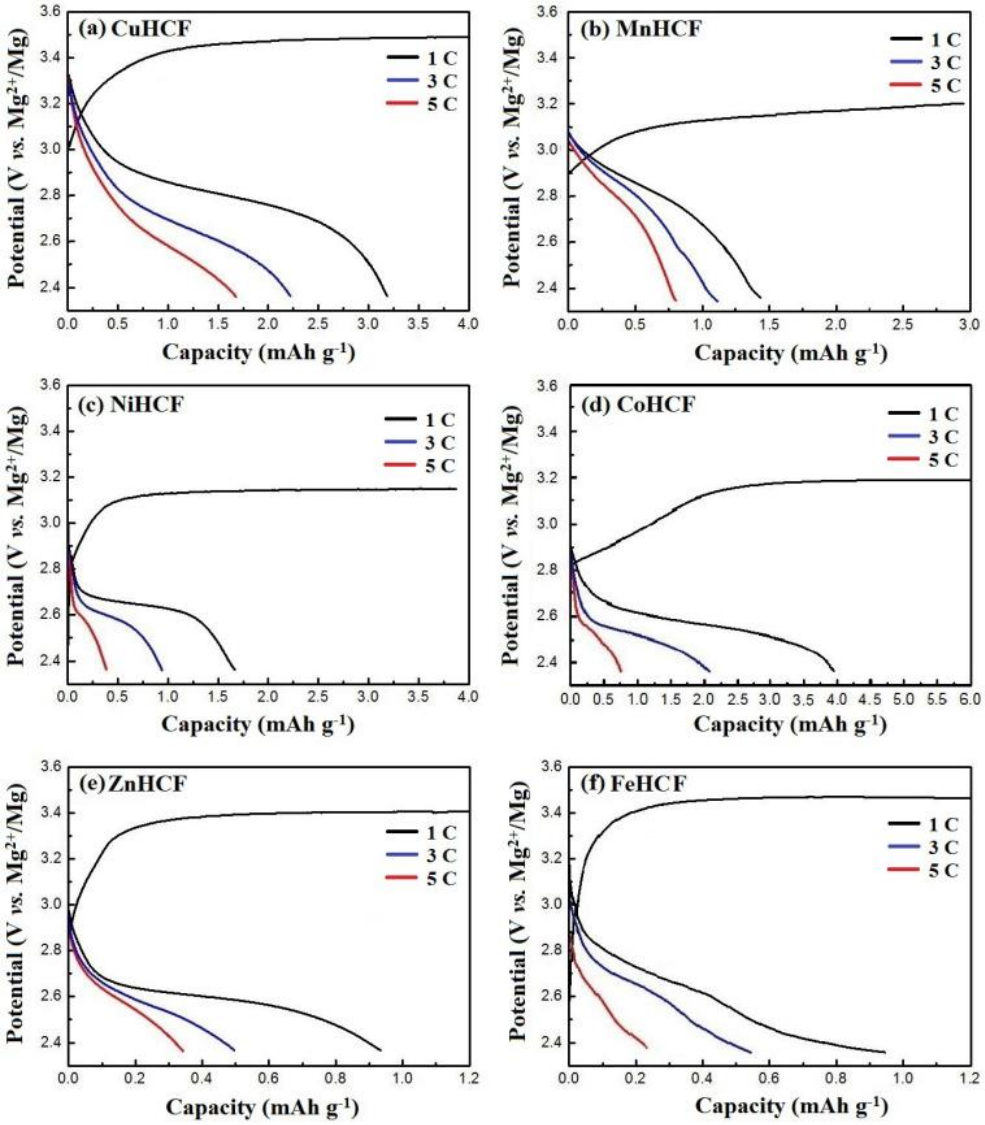


**Figure 6.** Charge and discharge curves at various discharge current densities.

This confirms the assumption that structures of this type have a greater tendency to pass charged cations. The optimum charge/discharge current density was calculated from the cyclic voltammetry results and the capacitance values for each sample. The results of testing the samples at constant current are shown in Figure 6. The experimental and theoretical capacitance values are quite close. A large difference is observed for FeHCF, CoHCF and ZnHCF. A larger value is the equilibrium potential. For samples containing potassium, the value of the equilibrium potential is higher: NiHCF (8.3 mol% K vs. Ni) 2.68 V, CuHCF (9.8 mol% K vs. Cu) 2.80 V, MnHCF (15.1 mol% K vs. Mn) 2.81 V. The equilibrium potential for samples without potassium is FeHCF 2.65 V, CoHCF 2.60 V, ZnHCF 2.59 V.

## 5. Conclusions

In conclusion, we note that the nature of 3d-metals dramatically affects the physicochemical properties of the PB-analogues. PB-analogue with zinc differs from other samples by the crystal lattice.

**Table 6.** Comparison of polarizing ability of six-coordinated metals ions in PB-analogues structure.

| Ion | Spin | Crystalline radius (Å) | Polarizing ability ($Å^{-1}$) | $Q_{exp}$ (mAh/g) |
|---|---|---|---|---|
| $Fe^{+2}$ | low | 0.75 | 2.67 | 2 |
| $Co^{+2}$ | low | 0.79 | 2.53 | 6 |
| $Mn^{+2}$ | low | 0.81 | 2.47 | 10 |
| $Ni^{+2}$ | – | 0.83 | 2.41 | 19 |
| $Mg^{+2}$ | – | 0.86 | 2.33 | – |
| $Cu^{+2}$ | – | 0.87 | 2.30 | 21 |
| $Zn^{+2}$ | – | 0.88 | 2.27 | 2 |
| $K^{+}$ | – | 1.52 | 0.66 | – |
| $Fe^{+2}$ | low | 0.75 | 2.67 | 2 |
| $Co^{+2}$ | low | 0.79 | 2.53 | 6 |

We improve an explanation of the magnesium ions intercalation processes into PB-analogues structure taking into account not only ions size but of 3d-metals and magnesium ions. Thus, value of polarizing ability magnesium ion which surround with six water molecules is similar that for 3d-metals correlates with increased experimental capacitance magnitude (Table 6) for the samples which contain Ni and Co ions. In connection with this, it becomes urgent to investigate complexes containing magnesium ions as cathode materials for Mg-ion batteries.

**Author Contributions:** Conceptualization, A.P. and A.S.; methodology, A.S.; software, S.E.; validation, A.A.; formal analysis, I.P.; investigation, S.E.; resources, A.F.; data curation, S.E.; writing—original draft preparation, A.S.; writing—review and editing, S.E.; visualization, A.A.; supervision, A.P.; project administration, A.S.; funding acquisition, A.P. All authors have read and agreed to the published version of the manuscript.

**Funding:** The authors acknowledge Saint-Petersburg State University for research grant №**102591880** that provided financial support for the development and characterization.

**Acknowledgments:** The scientific research was performed at the Research park of St. Petersburg State University: Centre for Geo-Environmental Research and Modeling (GEOMODEL); Centre for Innovative Technologies of Composite Nanomaterials; Magnetic Resonance Research Centre; Chemical Analysis and Materials Research Centre; Centre for Optical and Laser Materials Research; Centre for Molecular and Cell Technologies; Centre for X-ray Diffraction Studies; Thermogravimetric and Calorimetric Research Centre; Centre for Physical Methods of Surface Investigation; Centre for Diagnostics of Functional Materials for Medicine, Pharmacology and Nanoelectronics; and Nanophotonics Centre.

**Conflicts of Interest:** The authors declare no conflicts of interest.

## References


1. Krap, C.P.; Balmaseda, J.; Castillo, L.F.; Zamora, B.; Reguera, E. Hydrogen Storage in Prussian Blue Analogues: $H_2$ Interaction with the Metal Found at the Cavity Surface. *Energy Fuels* **2010**, *24* 24, 581−589.
2. Kaye, S.S.; Long, J.R. Hydrogen Storage in the Dehydrated Prussian Blue Analogues $M_3[Co(CN)_6]_2$ (M = Mn, Fe, Co, Ni, Cu, Zn). *J. Am. Chem. Soc.* **2005**, *127*, 6506−6507.
3. Matsui, J.; Kikuchi, R.; Miyashita, T. A Trilayer Film Approach to Multicolor Electrochromism. *J. Am. Chem. Soc.* **2014**, *136*, 842−845.
4. Torad, N.L.; Hu, M.; Imura, M.; Naito, M.; Yamauchi. Large Cs adsorption capability of nanostructured Prussian Blue particles with high accessible surface areas. *Y. J. Mater. Chem.* **2012**, *22*, 18261−18267.
5. Aguila, D.; Prado, Y.; Koumousi, E.; Mathoniere, C.; Clerac, R. Switchable Fe/Co Prussian blue networks and molecular analogues. *Chem. Soc. Rev.* **2016**, *45*, 203−224.
6. Long, J.; Guari, Y.; Guerin, C.; Larionova, J. Prussian blue type nanoparticles for biomedical applications. *Dalton Trans* **2016**, *45*, 17581−17587.
7. Dharman, M.M.; Yu, J.-I.; Ahn, J.-Y.; Park, D.-W. Selective production of cyclic carbonate over polycarbonate using a double metal cyanide–quaternary ammonium salt catalyst system. *Green Chem.* **2009**, *11*, 1754−1757.
8. Srivastava, R.; Srinivas, D.; Ratnasamy, P. Fe–Zn double-metal cyanide complexes as novel, solid transesterification catalysts. *J. Catal.* **2006,** *241*, 34−44.
9. Zakaria, M.B.; Hu, M.; Hayashi, N.; Tsujimoto, Y.; Ishihara, S.; Imura, M.; Suzuki, N.; Huang, Y.-Y.; Sakka, Y.; Ariga, K.; Wu, K.C.-W.; Yamauchi, Y. Thermal Conversion of Hollow Prussian Blue Nanoparticles into Nanoporous Iron Oxides with Crystallized Hematite Phase. *Eur. J. Inorg. Chem.* **2014**, 1137−1141.
10. Zhang, L.; Shi, L.; Huang, L.; Zhang, J.; Gao, R.; Zhang, D. Rational Design of High-Performance $DeNO_x$ Catalysts Based on $Mn_xCo_{3-x}O_4$ Nanocages Derived from Metal–Organic Frameworks. *ACS Catal.* **2014**, *4*, 1753−1763.
11. Wessells, C.D.; Peddada, S.V.; McDowell, M.T.; Huggins, R.A.; Cui, Y. The Effect of Insertion Species on Nanostructured Open Framework Hexacyanoferrate Battery Electrodes. J. Electrochem. Soc. 2012, 159, A98−A103.
12. Omarova, M.; Koishybay, A.; Yesibolati, M.; Mentbayeva, A.; Umirov, N.; Ismailov, K.; Adair, D.; Baba, M.; Kurmanbayeva, I.; Bakenov, Z. Nickel Hexacyanoferrate Nanoparticles as a Low Cost Cathode Material for Lithium-Ion Batteries. *Electrochim. Acta* **2015**, *184*, 58−63.
13. Wang, R.; Shyam, B.; Stone, K.; Weker, J.; Pasta, M.; Lee, H.; Toney, M.; Cui, Y. Reversible Multivalent (Monovalent, Divalent, Trivalent) Ion Insertion in Open Framework Materials. *Adv. Energy Mater.* **2015**, *1401869*, 1−10.
14. Wessells, C.; Huggins, R.; Cui, Y. Copper hexacyanoferrate battery electrodes with long cycle life and high power. *Nat. com.* **2011**, *2*, 1−5.
15. Sun, X.; Ji, X.; Zhou, Y.; Shao, Y.; Zang, Y.; Wen, Z.; Chen, C. A new gridding cyanoferrate anode material for lithium and sodium ion batteries: $Ti_{0.75}Fe_{0.25}[Fe(CN)_6]_{0.96}{\cdot}1.9H_2O$ with excellent electrochemical properties. *J. Power Sources* **2016**, *314*, 35−38.
16. Zhang, Q.; Fu, L.; Luan, J.; Huang, X.; Tang, Y.; Xie, H.; Wang, H. Surface engineering induced core-shell Prussian blue@polyaniline nanocubes as a high-rate and long-life sodium-ion battery cathode. *J. Power Sources* **2018**, *395*, 305−313.
17. Ke, X.; Zhao, Z.; Liu, J.; Shi, Z.; Li, Y.; Zhang, L.; Zhang, H.; Chen, Y.; Guo, Z.; Wu, Q; Liu, L. Improvement in capacity retention of cathode material for high power density lithium ion batteries: The route of surface coating. *Applied Energy* **2017**, *194*, 540−548.
18. Yabuuchi, N.; Kubota, K.; Dahbi, M.; Komaba, S. Research Development on Sodium-Ion Batteries. *Chem. Rev.* **2014**, *114*, 11637.
19. Yoo, H.; Shterenberg, I.; Gofer, Y.; Gershinsky, G.; Pour, N.; Aurbach, D. Mg rechargeable batteries: an on-going challenge. *Energy Environ. Sci.* **2013**, *8*, 2265−2279.
20. Matthew, M.; Bock, D.; Takeuchi, E.; Marschilok, A.; Takeuchi, K. Cathode materials for magnesium and magnesium-ion based batteries. *Coord. Chem. Rev.* **2015**, *287*, 15−27.
21. Levi, E.; Mitelman, A.; Aurbach, D.; Brunelli, M.; Structural Mechanism of the Phase Transitions in the Mg−Cu−Mo6S8 System Probed by ex Situ Synchrotron X-ray Diffraction. *Chem. Mater.* **2007**, *19*, 5131−5142.
22. Levi, E.; Gershinsky, G.; Aurbach, D.; Isnard, O. Crystallography of Chevrel Phases, $MMo_6T_8$ (M = Cd, Na, Mn, and Zn, T = S, Se) and Their Cation Mobility. *Inorg. Chem.* **2009**, *48*, 8751−8758.
23. Levi, E.; Gofer, Y.; Aurbach, D. On the Way to Rechargeable Mg Batteries: The Challenge of New Cathode Materials. *Chem. Mater.* **2010**, *22*, 860−868.
24. Peng, B.; Liang J.; Tao, Z.; Chen, J. Magnesium nanostructures for energy storage and conversion. *J. Mater. Chem.*, **2009**, *19*, 2877−2883.
25. Wessells, C.; McDowell, M.; Peddada, S.; Pasta, M.; Huggins, R.; Cui, Y. Tunable Reaction Potentials in Open Framework Nanoparticle Battery Electrodes for Grid-Scale Energy Storage. ACS Nano **2012**, *6*, 1688−1694.
26. Yang, D.; Xu, J.; Liao, X.-Z.; Wang, H.; He, Y.-S.; Ma, Z.-F. Retracted Article: Prussian blue without coordinated water as a superior cathode for sodium-ion batteries. Chem. Com. **2015**, *51*, 8181−8184.
27. Liu, S.; Pan, G.; Li, G.; Gao, X.P. Copper hexacyanoferrate nanoparticles as cathode material for aqueous Al-ion batteries. *J. Mat. Chem. A* **2015**, *3*, 959−962.
28. Mizuno, Y.; Okubo, M.; Hosono, E.; Kudo, T.; Oh-ishi, K.; Okazawa, A.; Kojima, N.; Kurono, R.; Nishimura, S.; Yamada, A. Electrochemical $Mg^{2+}$ intercalation into a bimetallic CuFe Prussian blue analog in aqueous electrolytes. *J. Mater. Chem. A* **2013**, *1*, 13055−13059.

29. Wang, R.; Wessells, C.; Huggins, R.; Cui, Y. Highly Reversible Open Framework Nanoscale Electrodes for Divalent Ion Batteries. *NanoLett.* **2013**, *13*, 5748−5752.
30. Mizuno, Y.; Okubo, M.; Hosono, E.; Kudo, T.; Zhou, H.; Oh-ishi, K. Suppressed Activation Energy for Interfacial Charge Transfer of a Prussian Blue Analog Thin Film Electrode with Hydrated Ions ($Li^+$, $Na^+$, and $Mg^{2+}$). *J. Phys. Chem. C*, **2013**, *117*, 10877−10882.
31. Robin, M.; Day, P. Mixed Valence Chemistry-A Survey and Classification. *Adv. Inorg. Chem. Radiochem.* **1968**, *10*, 247−422.
32. Li, Q.; Kharzeev, D.; Zhang, C. et al. Chiral magnetic effect in $ZrTe_5$. *Nature Phys* **2016**, *12*, 550–554.
33. Ling, C.; Chen, J.; Mizuno, F. First-principles study of alkali and alkaline earth ion intercalation in iron hexacyanoferrate: the important role of ionic radius. *J. Phys. Chem. C.* **2013**, *117*, 21158–21165.
34. Lipson, A.; Pan, B.; Lapidus, S.; Liao, C.; Vaughey, J.; Ingram, B. Rechargeable Ca-ion batteries: a new energy storage system. *Chem. Mater.* **2015**, *27*, 8442–8447.
35. Imanishi, N.; Morikawa, T.; Kondo, J.; Takeda, Y.; Yamamoto, O.; Kinugasaand, N.; Yamagishi, T. Lithium intercalation behavior into iron cyanide complex as positive electrode of lithium secondary battery. J. Pow. Sourc. **1999**, *79*, 215–219.
36. Kim, H.; Hong, J.; Park, K.-Y.; Kim, H.; Kim, S.-W.; Kang, K. Aqueous rechargeable Li and Na ion batteries. *Chem. Rev*. **2014**, *114*, 11788–11827.
37. Padigi, P.; Thiebes, J.; Swan, M.; Goncher, G.; Evans, D.; Solanki, R. Prussian Green: a high rate capacity cathode for potassium ion batteries. *Electrochim. Acta*. **2015**, *166*, 32–39.
38. Nie, P.; Shen, L.; Luo, H.; Ding, B.; Xu, G.; Wang, J.; Zhang, X. Prussian blue analogues: a new class of anode materials for lithium ion batteries. *J. Mater. Chem. A*. **2014**, *2*, 5852–5857.
39. Christensen, P.; Hamnett, A.; Higgins, S. A study of electrochemically grown Prussian blue films using Fourier-transform infrared spectroscopy. *J. Chem. Soc. Dalton Trans.* **1990**, *9*, 2233–2238.
40. Eftekhari, A. Potassium secondary cell based on Prussian blue cathode. *J. Power Sources*. **2004**, *126*, 221–228.
41. Yagi, S.; Fukuda, M.; Makiura, R.; Ichitsubo, T.; Matsubara, E. EQCM analysis of redox behavior of Prussian blue in a lithium battery electrolyte. *J. Mater. Chem. A.* **2014**, *2*, 8041–8047.
42. Trocoli, R.; Mantia, F.L. An Aqueous Zinc-ion battery based on copper hexacyanoferrate. *ChemSusChem*. **2015**, *8*, 481–485.
43. Reed, L.; Ortiz, S.; Xiong, M.; Menke, E. A rechargeable aluminum-ion battery utilizing a copper hexacyanoferrate cathode in an organic electrolyte. *Chem. Commun.* **2015**, *51*, 14397–14400.
44. Bock, C.; Kaufman, A.; Glusker, J. Coordination of water to magnesium cations. *Inorg. Chem.* **1994**, *33*, 419−427.